Asymmetric Magnetic Reconnection in the Solar Corona:

Simulation vs. Observation

Drake A. Ranquist

A senior thesis submitted to the faculty of
Brigham Young University
in partial fulfillment of the requirements for the degree of

Bachelor of Science

Dr. Victor Migenes, Dr. Nick Murphy, and Dr. Mari Paz Miralles, Advisors

Department of Physics and Astronomy

Brigham Young University

April 2013

ABSTRACT

Asymmetric Magnetic Reconnection in the Solar Corona:
Simulation vs. Observation

Drake A. Ranquist
Department of Physics and Astronomy
Bachelor of Science

Magnetic reconnection is the leading mechanism for energy release in solar eruptions. The coronal magnetic field cannot be measured remotely or *in situ*, which makes modeling difficult. Using NIMROD, an extended magnetohydrodynamics simulation code, we have developed an indirect method to obtain the asymmetry of the magnetic field during observed solar eruptions. We analyzed the eruptions on 6/7 Dec 2010 and 7 Mar 2011 with the Atmospheric Imaging Assembly. We traced post-flare loops and found the asymmetric reconnection models that best fit the observations using rotation and chi-squared algorithms. To further constrain the results, we rotated these fits onto the observations from the Solar Terrestrial Relations Observatory. We estimated that the 2010 event had a magnetic field asymmetry of 4:1 and the 2011 event an asymmetry of 1.5:1. In combination with other signatures of asymmetric magnetic reconnection, this can yield a method for determining the upstream magnetic field ratios during solar eruptions.

ACKNOWLEDGMENTS

Contents

List of Figures

List of Tables

Chapter 1

Introduction

1.1   Why Study Solar Flares and Coronal Mass Ejections?

The Sun puts technology at risk. Cell phone communication, GPS tracking, and climate studies require the continual operation of space satellites. The world population also relies on the continual distribution of electricity. During a solar eruption, the Sun unleashes ionizing particles that create geomagnetic storms. The resulting aurorae are dazzling, but ionizing particles and changing magnetic fields damage electronics and generate currents on Earth's surface. If satellites do not shut down when a storm hits, they can be crippled permanently. Similarly on Earth's surface, induced currents through power lines can destroy transformers and cause blackouts.

Space weather forecasters attempt to predict geomagnetic storms, but find it difficult. Using the current understanding of solar eruptions, wind, and magnetic field, they develop simulations that propagate the material from the Sun out to Earth's orbit. These simulations are improving at predicting how an observed solar eruption will affect the Earth. However, they cannot preemptively determine when the solar eruption will occur, how strong it will be, or in which direction it will travel. In order to improve space weather forecasts, solar flares and coronal mass ejections (CMEs)

must be better understood. We aim to improve this understanding by comparing simulated solar eruptions to observed events.

1.2 Current Understanding of Solar Eruption Events

The Sun is extremely dynamic. Its surface, which can be seen by the naked eye, gives a false sense of quiescence. It only has a temperature of about 5700 K and is occasionally blemished by sunspots. The solar corona, on the other hand, is a chaotic environment of changing magnetic fields and fluctuating plasmas. These plasmas reach temperatures in excess of 10^6 K [e.g., McKenzie (2011)] (see Fig. 1.1). Originally, only solar eclipses exposed the corona. But, now space satellites continually monitor its visible, ultraviolet, and x ray radiation. These observations show that the plasmas outline the magnetic field in large coronal loops, which intermittently flare and eject material. We will refer to these solar flares and coronal mass ejections as solar eruptions in this thesis.

It is the current understanding that during solar eruptions, magnetic reconnection converts magnetic energy into kinetic and thermal energy through the rearrangement of the magnetic field (Zweibel & Yamada 2009). Where anti-parallel magnetic fields lines meet, the magnetic field strength goes to zero. This allows the field lines to reconnect, as shown in Fig. 1.2. Upon reconnecting, the magnetic tension (a force density of the field line curvature) is very high. To understand magnetic tension, consider a simple rubber band analogy. When stretched, the rubber band is given potential energy in the form of tension. When released, the tension energy is converted into kinetic energy. Similarly, when magnetic tension is released, the plasma it carries is accelerated.

The current model of solar eruptions is shown in Fig. 1.3. Large coronal loops are pinched together and change connectivity through magnetic reconnection. This creates a self-contained
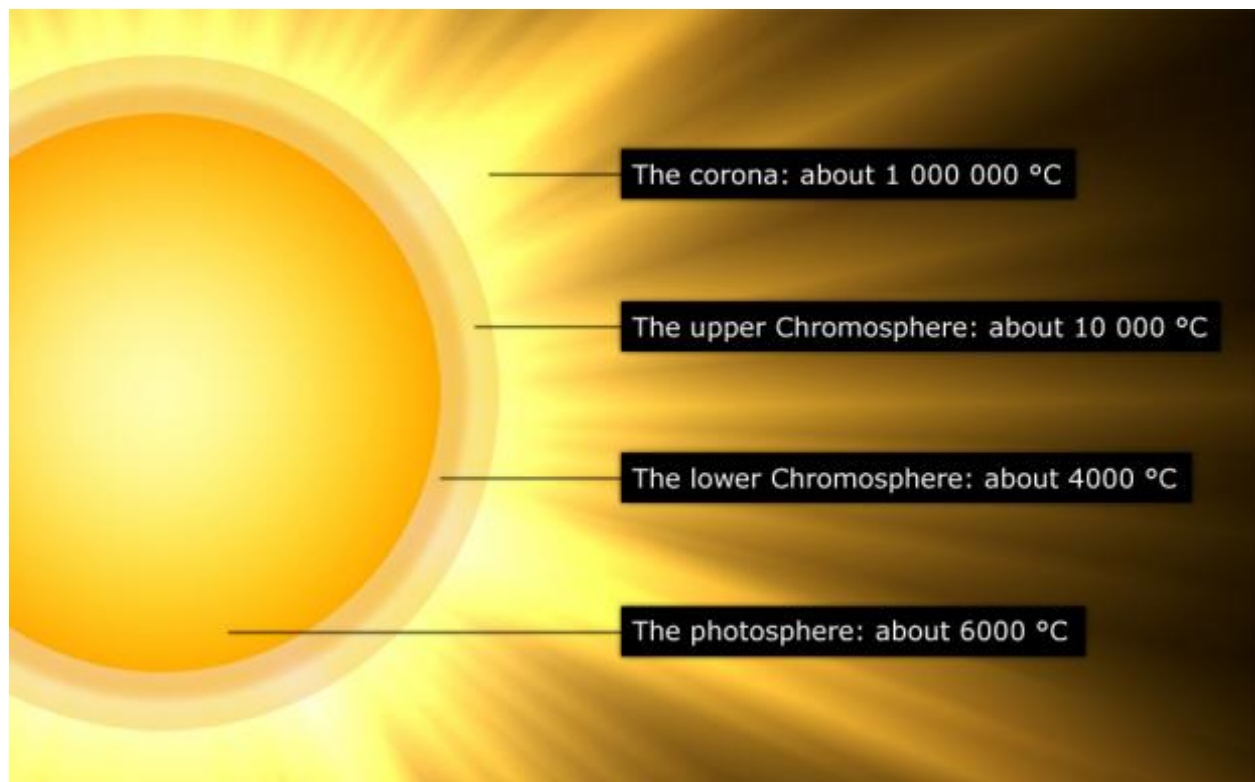
Figure 1.1 Temperatures of the solar surface and atmosphere. The surface of the Sun is called the photosphere. The two layers of atmosphere above the photosphere are the chromosphere and the corona. Temperatures reach a minimum in the lower chromosphere, but increase into the upper chromosphere. The corona is more diffuse than the chromosphere, but significantly hotter. Credit: Per Byhring.
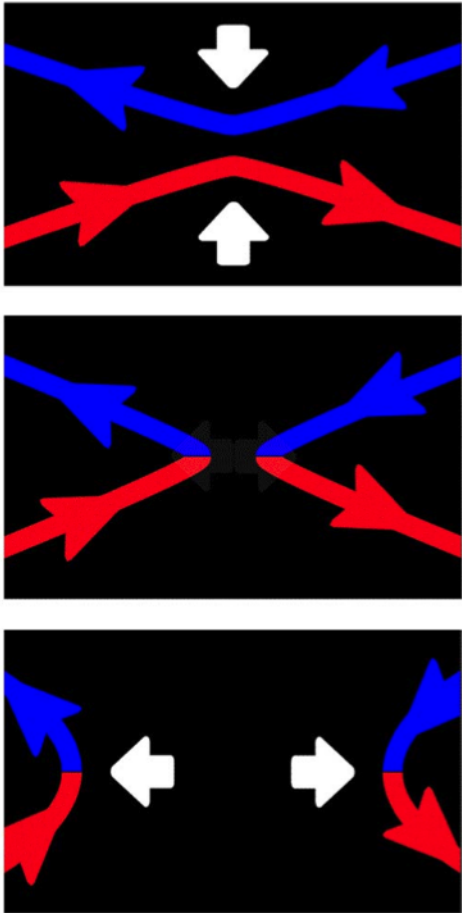
Credits: Center for Visual computing, Univ. of California Riverside

Figure 1.2 A diagram representing magnetic reconnection in two dimensions. The point of reconnection is known as the x-line. Magnetic tension accelerates particle outflows as the magnetic field relaxes.

plasmoid which rises away from the solar surface, propelled by the transfer of magnetic tension energy to plasma kinetic energy. At the x-line (the point of reconnection), inflowing plasma is rapidly ejected along a current sheet both away from the solar surface and towards it. The plasma interacts with the newly formed coronal loops and creates intense ultraviolet and x ray emission. These bright post-flare loops outline the magnetic field and reveal its shape.

1.3   Simulations of Magnetic Reconnection

Plasmas are extremely difficult to simulate. In some ways, plasmas act like fluids, which are described by hydrodynamics. But, charged particles create electric and magnetic fields as they move. The fields in turn affect the motion of the particles. These effects require Maxwell's equations. Magnetohydrodynamics (MHD) couples fluid hydrodynamics with Maxwell's equations to characterize plasmas.

A team at the University of Wisconsin-Madison headed an effort to simulate laboratory and astrophysical plasmas. They named the code they developed NIMROD, which stands for "Non-Ideal Magnetohydrodynamics with Rotation and Other Doohickies" (NIMROD) (Sovinec et al. 2004). This code uses modified MHD equations which account for a variety of non-ideal effects, including resistivity. Murphy et al. (2012) describes in detail the equations used to generate the simulations we use in this paper.

To simulate magnetic reconnection in the solar corona using NIMROD, we must make several assumptions. We first assume that the magnetic fields are line-tied. This means that the locations where magnetic fields meet the solar surface (known as footpoints) do not move. They are tied to the solar surface. This is a very good assumption because the Sun is highly conductive (Zweibel & Yamada 2009). Murphy et al. (2012) used a conductive wall boundary condition to simulate the solar surface.
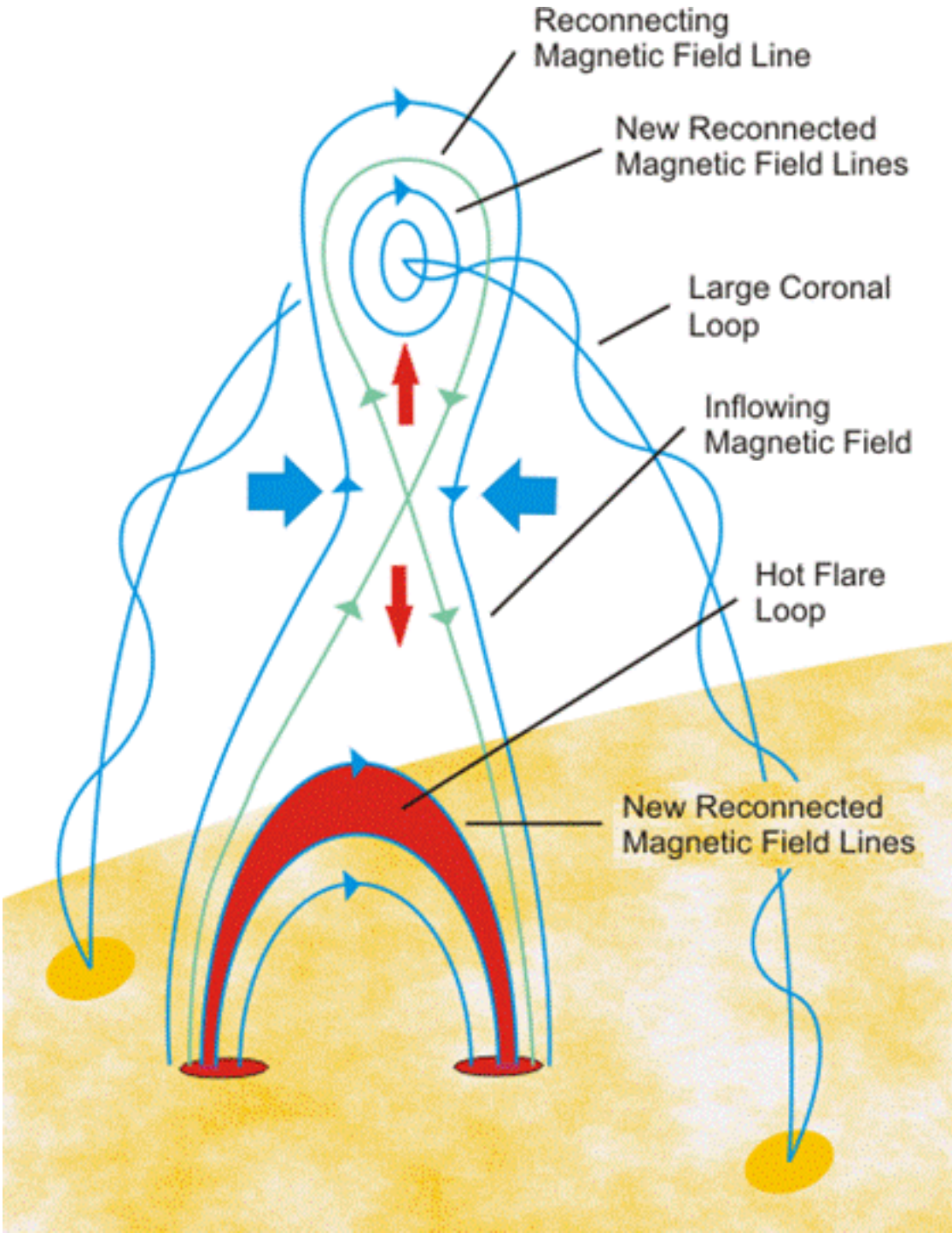
Figure 1.3 The current model of solar eruptions. Magnetic reconnection ejects a plasmoid and forms post-flare loops. Credit: University of California, Berkeley.

The NIMROD simulations are two-dimensional, and are computationally intensive. A three-dimensional simulation would require more than the allotted computational resources to Murphy et al. This forces us to assume that there are no three-dimensional effects during magnetic reconnection and that the magnetic fields are isolated from other systems in the solar corona. We seek to determine the validity of these assumptions for future research.

1.4 Observations of Magnetic Reconnection

Magnetic reconnection occurs at small scales—tens to hundreds of meters. These are too small to resolve with a telescope and cannot be observed directly. Even so, the corona exhibits many indirect signatures of magnetic reconnection. Elongated current sheets have been detected in the wake of CMEs (Ciaravella et al. 2002). Sudden loop linkages connect separate active regions (McKenzie 2011). Flares create supra-arcade downflows, which are voids flowing downward towards the solar surface above the post-flare loops (Warren et al. 2011). Solar physicists now generally accept magnetic reconnection as a key process in solar eruptions because of this evidence.

Magnetic field asymmetries have also been detected during magnetic reconnection. Laboratory experiments have shown asymmetries in the inflow direction (Yamada et al. 1997). The same has been observed in Earth's dayside magnetopause (where the solar wind meets Earth's magnetic field)(Phan & Paschmann 1996). One spectacular solar eruption that exhibited asymmetries was named the "Cartwheel CME." The rising plasmoid showed apparent rotation while the current sheet drifted with time (Savage et al. 2010).

We chose to study two solar eruptions that demonstrated features of asymmetric magnetic reconnection. We chose these events because the Hinode X-Ray Telescope (XRT) recorded candle-like cusps pointing towards x-lines (see Fig. 1.4 & 1.5) (Golub et al. 2007). The first began on 6 Dec 2010 and ended early the next day. The rolling motions of this event have been well analyzed
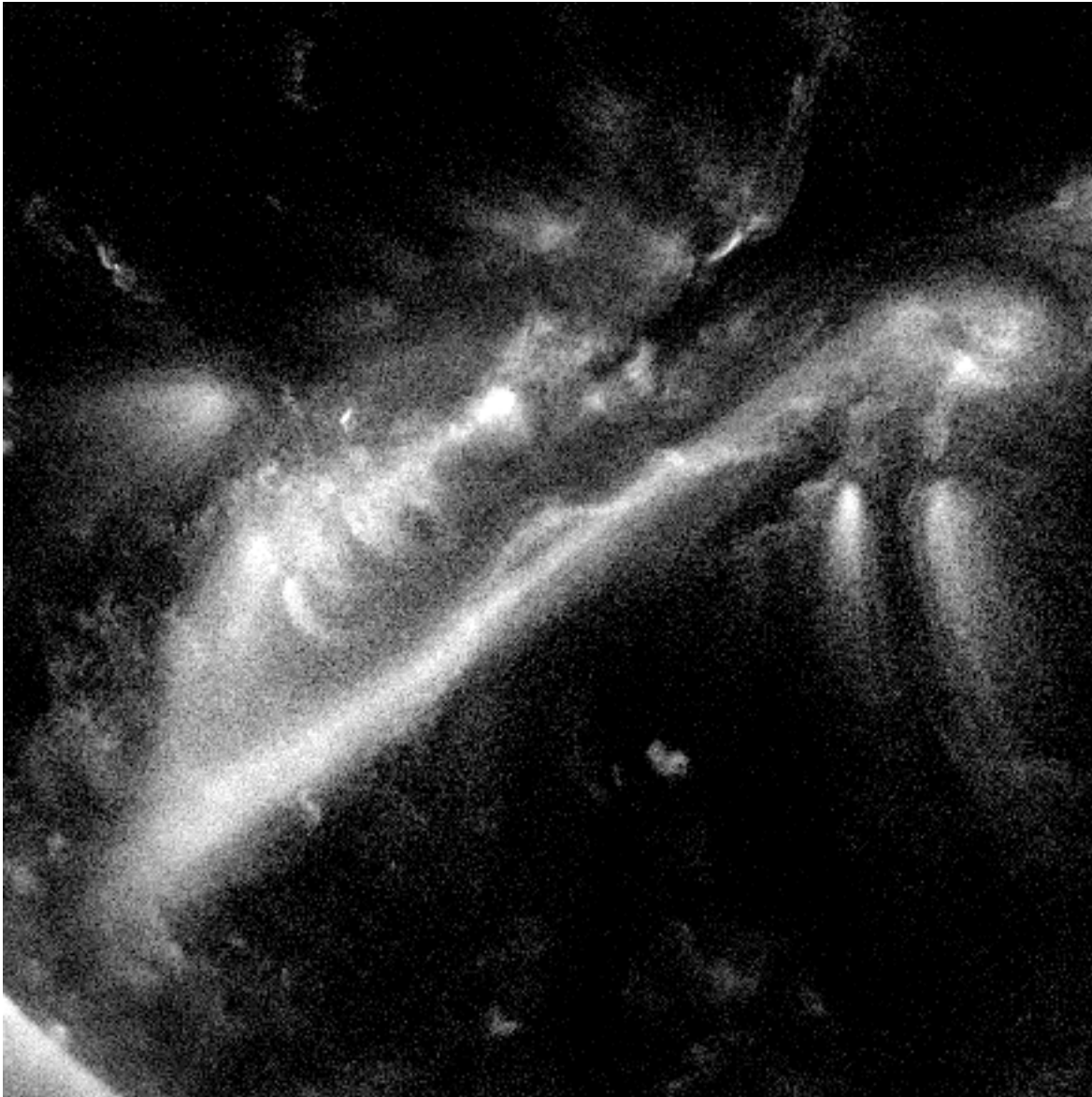
Figure 1.4 A Hinode X-Ray Telescope (XRT) image of the 6/7 Dec 2010 event. Note that the flaring region forms a candle-like cusp.
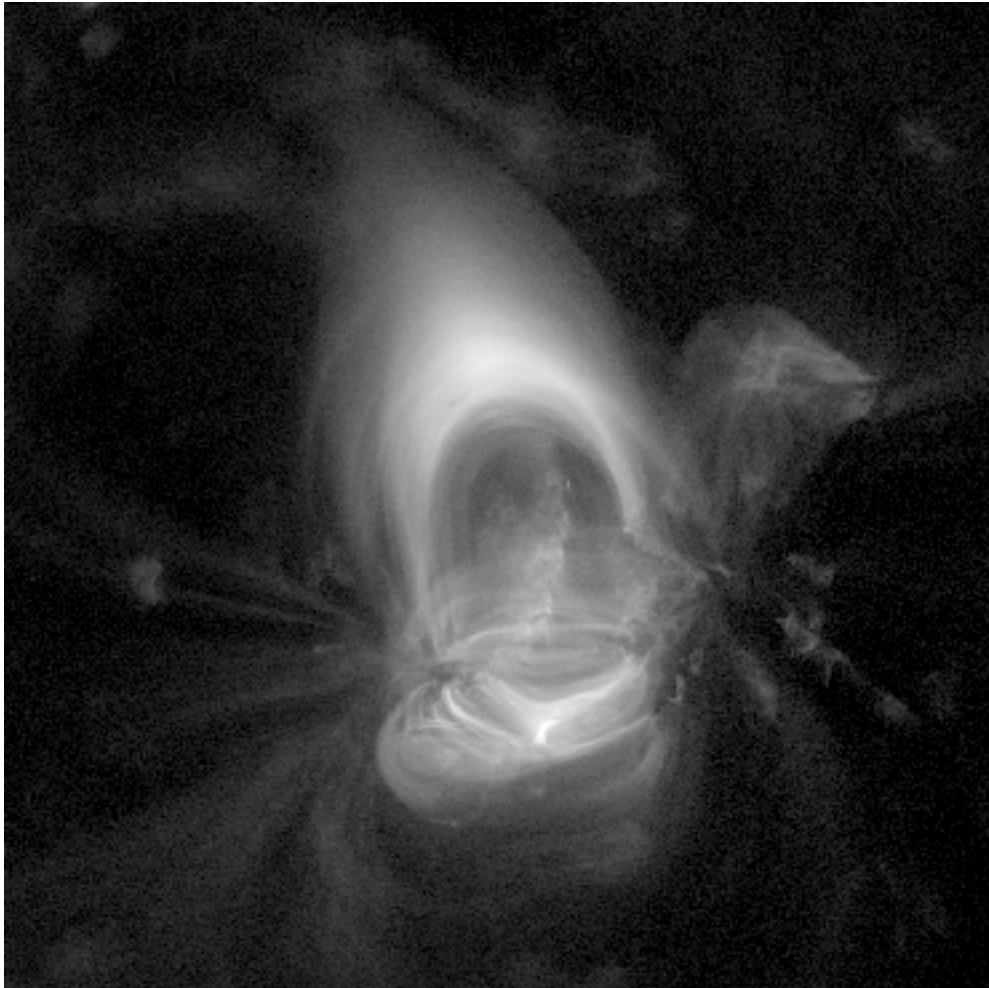
Figure 1.5 A Hinode X-Ray Telescope (XRT) image of the 7 Mar 2011 event. Note that the flaring region forms candle-like cusp.

by Su & van Ballegooijen (2013). The second event occurred on 7 Mar 2011.

1.5   Statement of Problem

Using the NIMROD simulations and ultraviolet images of the two identified observations, we address the following three questions:

1. Do we find evidence of asymmetric magnetic reconnection in solar observations?

2. How well do the simulations agree with observations?

3. Can we determine the magnetic field asymmetry during solar eruptions?

The last question is of particular interest because currently the coronal magnetic field cannot be measured. The Helioseismic Magnetic Imager (HMI) aboard the Solar Dynamics Observatory (SDO) probes the magnetic field of the photosphere in the form of magnetograms, but the magnetic field of the solar corona must be extrapolated. We developed an observational tool for obtaining an estimate of the magnetic field asymmetry during solar eruptions.

1.6   Overview

In this thesis, we compare line-tied MHD simulations to coronal observations of solar eruptions. We analyze two singular events that suggest asymmetric magnetic reconnection. We seek to determine the magnetic field asymmetry during these events. In Chapter 2, we will first discuss the simulations generated by Murphy et al. (2012). We then introduce the three spacecraft used to observe the eruption events. In Chapter 3, we describe the computational methods used to remove projection effects, superimpose the simulations onto the observations, and provide a goodness factor of the fits. In Chapter 4, we present the estimated asymmetries of the two solar eruption events and discuss future work.

Chapter 2

Data Obtained from Simulations and Observations

2.1 Simulation Data

The simulations were produced by Murphy et al. (2012) using the NIMROD code. An example of symmetric reconnection is shown in Fig. 2.1 and an example of asymmetric reconnection is shown in Fig. 2.2. Their simulations allowed for resistivity and anisotropic thermal conduction. They also used conducting wall boundary conditions. This ties all of the magnetic field lines to the boundaries. One boundary represents the photosphere, where magnetic field lines are tied to the solar surface. The other three boundaries are considered far enough away to not affect the results of the simulations. They produced simulations where the magnetic field asymmetries were 1:1, 1.25:1, 1.5:1, 2:1, 4:1, and 8:1. The simulation results are vector fields of the magnetic field, the density, the pressure, and other important quantities. Although we analyzed many of these quantities, we present simulation results of the magnetic field only.

When the asymmetric magnetic reconnection models are compared with symmetric models,
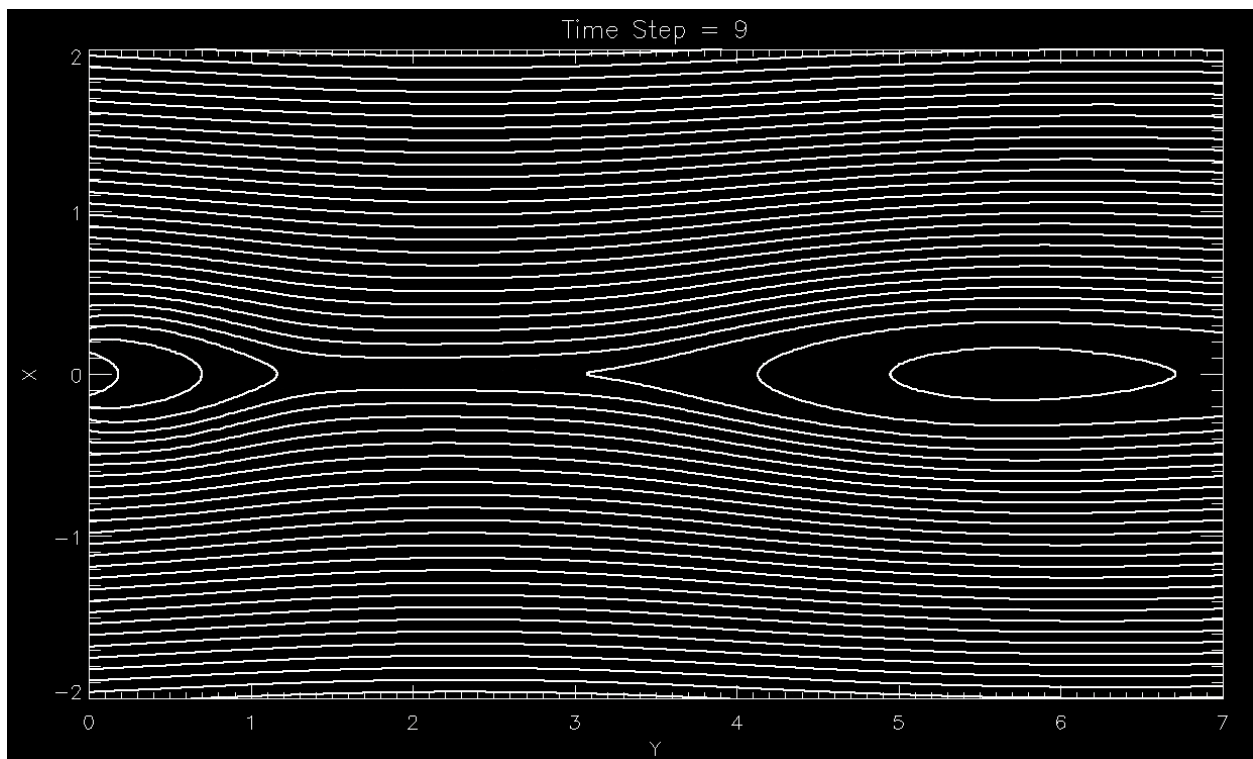
Figure 2.1 Simulation of symmetric magnetic reconnection. The contours of the magnetic field are shown. The magnetic field strength is equal for positive and negative values of X. The left boundary represents the solar surface, where newly connected post-flare loops are forming. At the (X,Y) coordinates $(0,5.7)$ is the rising plasmoid. Magnetic reconnection is occurring at $(0,2)$. The simulations contain a series of time steps. This shows time step number 9.
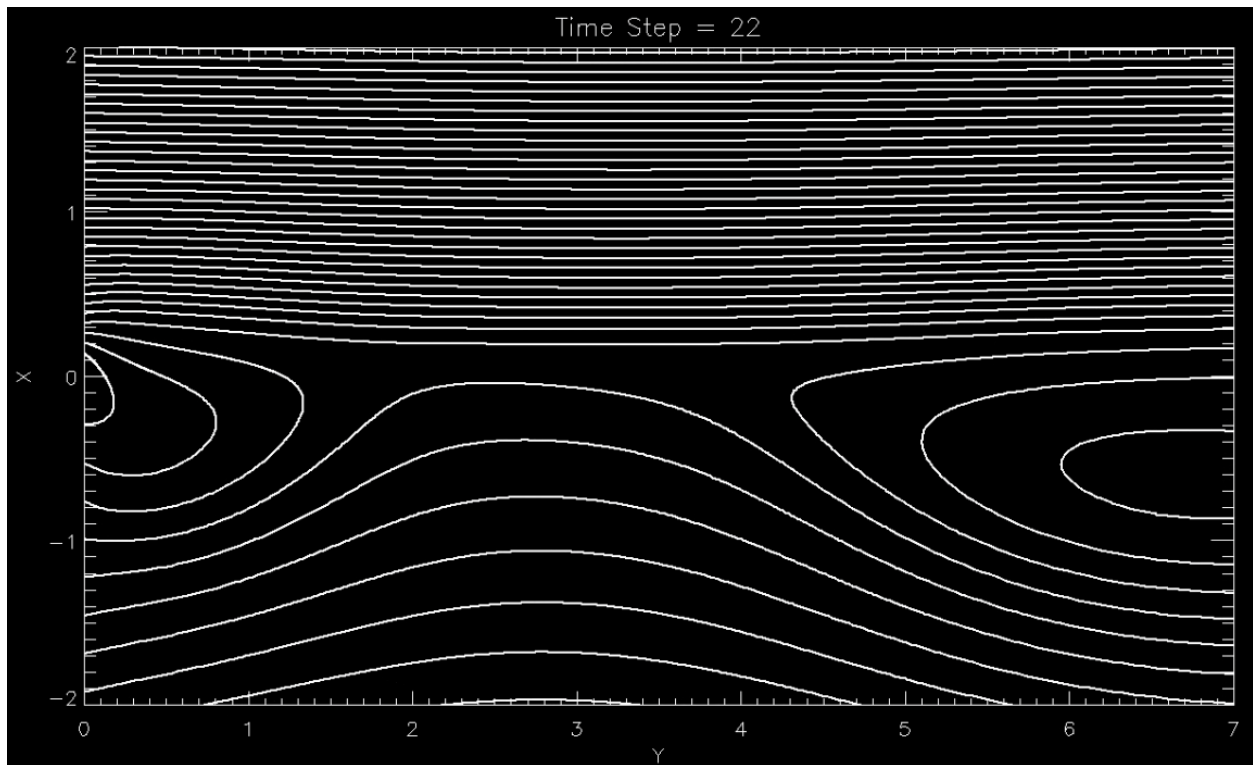
Figure 2.2 Simulation of asymmetric magnetic reconnection. The contours of the magnetic field are shown. This simulation had a magnetic field ratio of 4:1, where the positive *X* positions have a magnetic field strength four times greater than the negative *X* positions. The left boundary represents the solar surface, where newly connected post-flare loops are forming. At the (X, Y) coordinates $(-0.6, 6.9)$ is the rising plasmoid. The simulations contain a series of time steps. This shows time step number 22.

many signatures emerge which could be identified in observations. The signatures include distortion in the post-flare loops, asymmetric footpoint motion and brightness, off-axis location of the x-line, off-axis flow-stagnation point, asymmetric inflow velocities, drifting of the CME current sheet toward the strong-field upstream region, and circulation within the rising plasmoid. In this thesis, we focus solely on the distortion of post-flare loops.

2.2 Observational Data

We obtained observational data from three different instruments: the Atmospheric Imaging Array (AIA), the X-Ray Telescope (XRT), and the Solar Terrestrial Relations Observatory (STEREO). We will describe these instruments in the next three paragraphs.

AIA is a high cadence multi-wavelength telescope aboard the Solar Dynamics Observatory (SDO), which was launched into a geosynchronous orbit in February of 2010 (Pesnell et al. 2012). It takes full Sun exposures at eight wavelengths every 10 to 12 seconds (Lemen et al. 2012). Table 2.1 describes the atmospheric regions and plasma temperatures observed by the different filters. Although we obtained data from most of these filters, we will primarily present the 171 Å wavelength. This filter generally displays finer plasma structures.

XRT is a telescope aboard the Hinode spacecraft, which was formerly known as Solar-B. Solar-B was launched in September of 2006 (Kosugi et al. 2007). XRT does not image the full Sun, but is limited to a 30 arcmin field of view (Golub et al. 2007). It tracks active regions for x-ray flares with a typical cadence of two seconds between exposures. Using the Ti-poly and Al-mesh filters, we noted the candle-like cusps in both eruption events, which suggested asymmetric magnetic reconnection (see Fig. 1.4 & 1.5).

The STEREO mission uses two identical spacecraft to achieve a stereoscopic view of the Sun (Kaiser et al. 2008). They were launched in October of 2006 in opposite directions. One leads the

Filter Wavelength	Primary Ions	Region of Atmosphere	$\log(T)$
4500 Å	continuum	photosphere	3.7
1700 Å	continuum	temperature minimum, photosphere	3.7
304 Å	He II	chromosphere, transition region	4.7
1600 Å	C IV, continuum	transition region, upper photosphere	5.0
171 Å	Fe IX	quiet corona, upper transition region	5.8
193 Å	Fe XII, Fe XXIV	corona, hot flare plasma	6.2, 7.3
211 Å	Fe XIV	active-region corona	6.3
335 Å	Fe XVI	active-region corona	6.4
94 Å	Fe XVIII	flaring corona	6.8
131 Å	Fe VIII, Fe XXI	transition region, flaring corona	5.6, 7.0

Table 2.1 Atmospheric Imaging Assembly (AIA) filter characteristics, sorted by the temperature of detected ions (Lemen et al. 2012). Listed are the central wavelengths, the primary ions detected, the region of interest within the solar atmosphere, and the characteristic temperature of the detected ions. Some filters detect multiple ionic species at differing temperatures. Only eight of the ten filters can be used each exposure cycle.

Earth (STEREO-A) while the other trails the Earth (STEREO-B). The current locations of these two spacecraft can be found at stereo-ssc.nascom.nasa.gov/where.shtml, while Fig. 2.3 gives their locations at the time of the 2010 eruption. Our data comes from the Extreme Ultraviolet Imager (EUVI), which is a part of the Sun Earth Connection Coronal and Heliospheric Investigation (SEC-CHI) suite of instruments. Using these data, we have a second perspective of the same event. This allows us to remove projection effects that would otherwise occur when three-dimensional loops are projected onto a two-dimensional image.

Using these three instruments, we observed two separate solar eruption events (see Fig. 2.4 & 2.5). For both, we obtained data for a 12 hour period. The first erupted at 14:18 UT on 6 Dec 2010 and finished on 7 Dec 2010 (Su & van Ballegooijen 2013). It created a CME with a linear speed of 538 km/s. The second erupted at 14:15 UT on 7 Mar 2011. This created flaring, but did not lead to a CME.

These data were prepared using the SolarSoft system. This is a set of Interactive Data Language (IDL) software packages used to reduce the raw data from different solar instruments so that they can be analyzed. It also introduces a heliospheric coordinate system so that the locations of events observed from different instruments can be properly tracked.
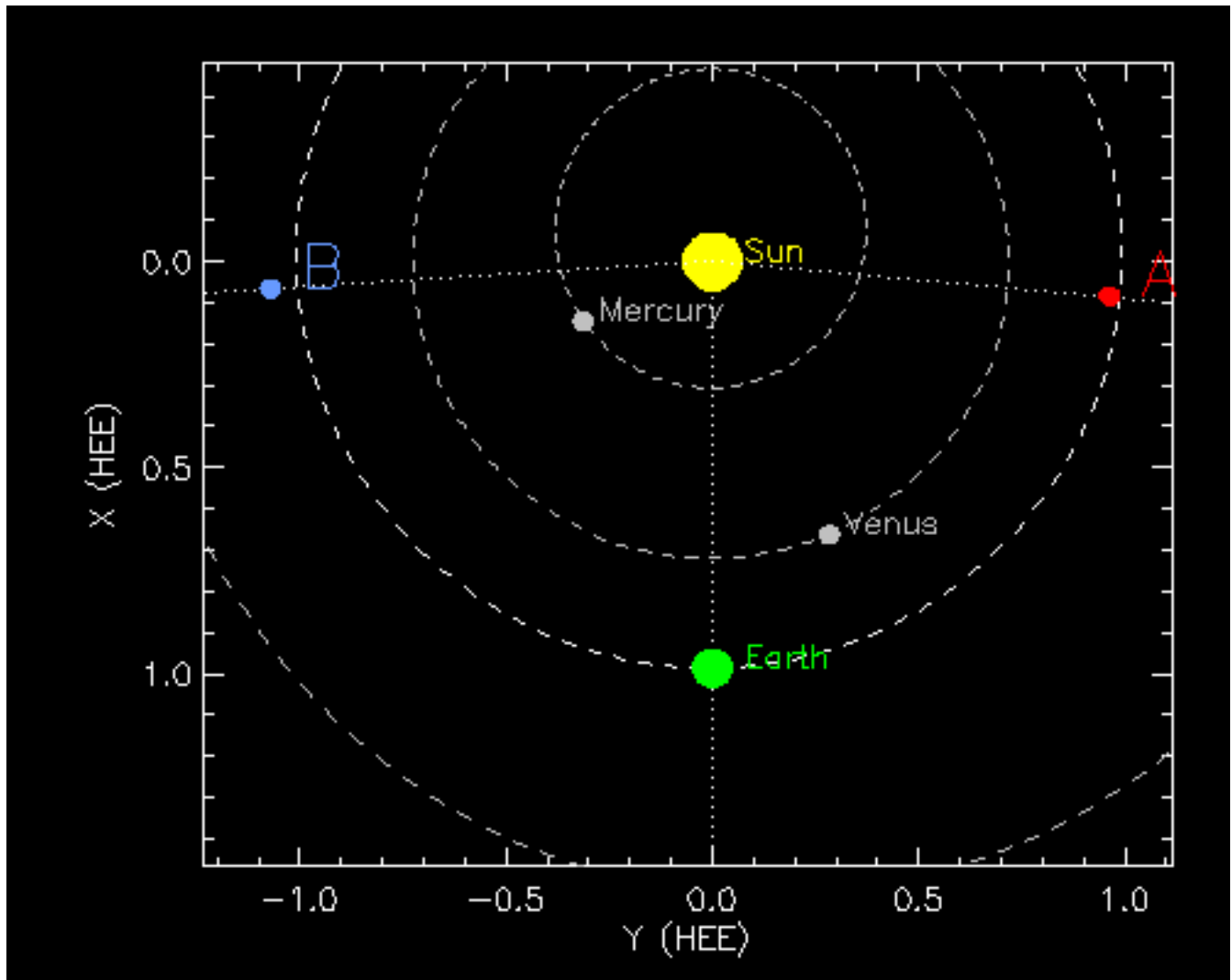
Figure 2.3 The Solar Terrestrial Relations Observatory (STEREO) spacecraft positions on 6 Dec 2010. These spacecraft were launched so that STEREO-A travels ahead of the earth and STEREO-B travels behind. They provide a stereoscopic view of the Sun. Credit: stereo-ssc.nascom.nasa.gov/where.shtml.
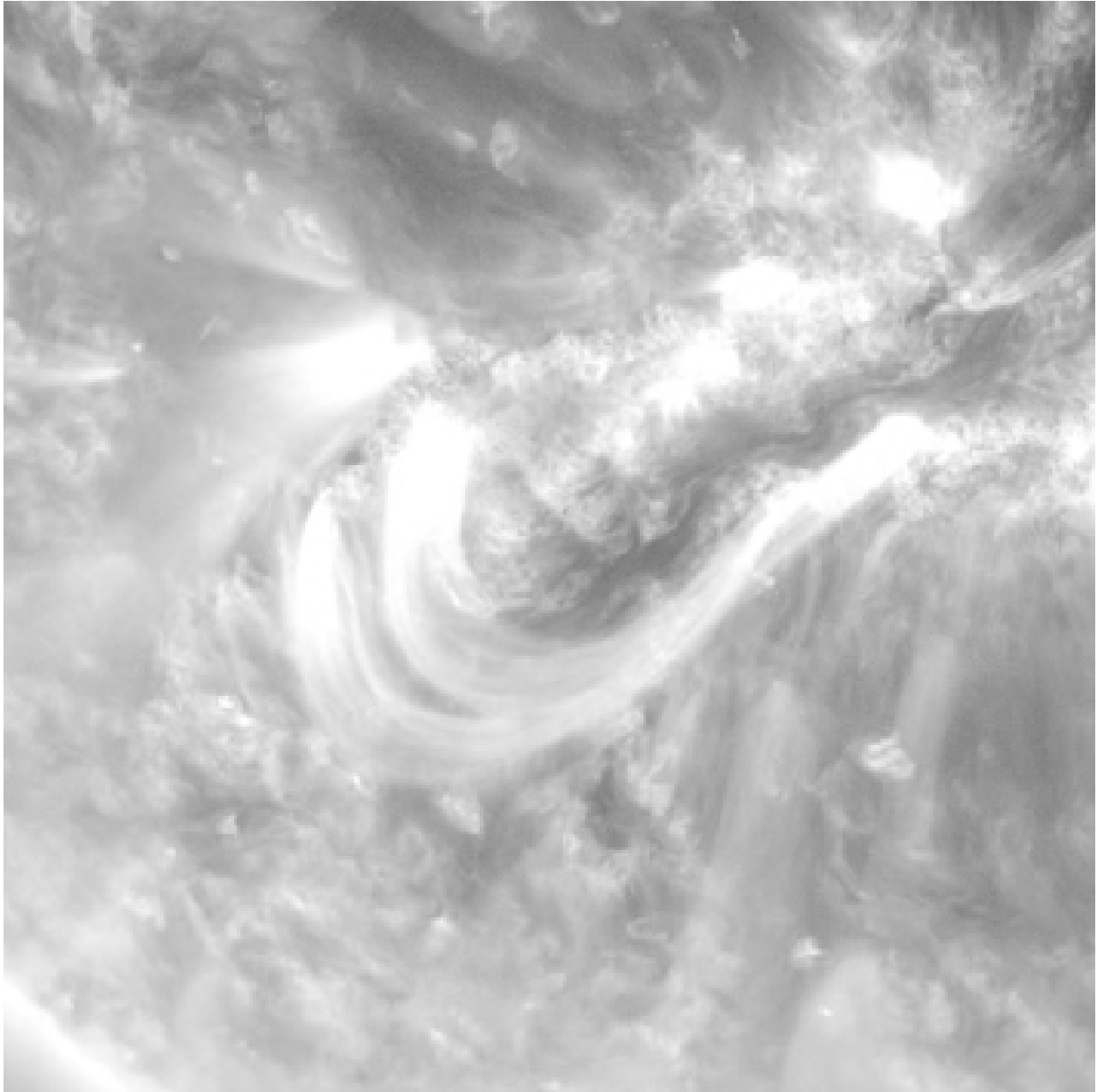
Figure 2.4 Post-flare loops of the 2010 Event taken with the Atmospheric Imaging Array (AIA) in 171 Å. This exposure is from UT 10:42 on December 7, 2010.
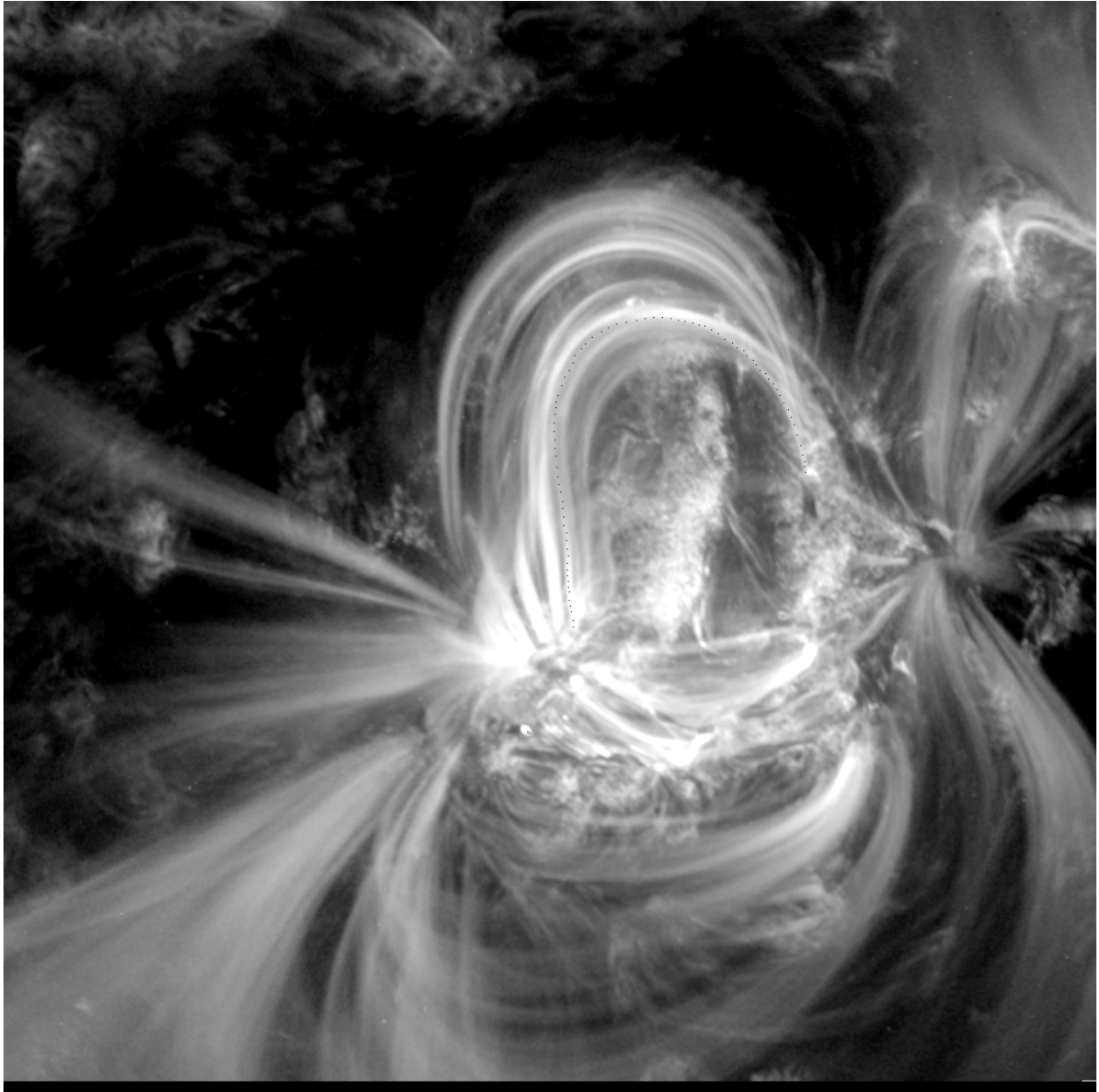
Figure 2.5 Post-flare loops of the 2011 Event taken with the Atmospheric Imaging Array (AIA) in 171 Å. This exposure is from UT 18:55 on March 7, 2011.

Chapter 3

Comparing the Simulations to the Observations

3.1 Extracting Simulated Post-Flare Loops

The simulations yield magnetic field vectors as a function of time. To extract the post-flare loops, we used Euler's method of numerical integration. This method was first described in *Institutionum calculi integralis*. We selected a position along the boundary and obtained the direction of the magnetic field. We stepped in this direction to a new point. We again obtained the direction of the magnetic field and stepped to a new point. This process continued until we returned to the boundary. The series of points formed a loop. We decreased the step size until there was no noticeable difference in the extracted loop shape.

Once we extracted the simulated post-flare loops, we analyzed projection effects by rotating them about the *x*, *y*, and *z* axes. The coronal observations project three dimensional loops onto a two dimensional plane. From these images alone, it is impossible to know the angle the loops make with respect to the solar surface. At certain angles, symmetric loops appear asymmetric. By

using the following rotation matrices

$$R_x(\theta) = \begin{bmatrix} 1 & 0 & 0 \\ 0 & \cos\theta & -\sin\theta \\ 0 & \sin\theta & \cos\theta \end{bmatrix}, R_y(\theta) = \begin{bmatrix} \cos\theta & 0 & \sin\theta \\ 0 & 1 & 0 \\ -\sin\theta & 0 & \cos\theta \end{bmatrix}, R_z(\theta) = \begin{bmatrix} \cos\theta & -\sin\theta & 0 \\ \sin\theta & \cos\theta & 0 \\ 0 & 0 & 1 \end{bmatrix},$$

we viewed symmetrical and asymmetrical post-flare loops from various angles, as shown in Figs. 3.1 & 3.2. We noted that asymmetrical loops have a straight edge on the strong magnetic field side and bulges out on the weak magnetic field side. Thus, we can distinguish between symmetrical and asymmetrical cases.

3.2   Tracing Observed Post-Flare Loops

We traced 19 observed post-flare loops using an IDL routine that records the mouse position when the loop is clicked. We selected distinct loops at various times and heights during the observed eruptions. The first and last positions clicked marked the footpoints. We recorded about 100 evenly spaced locations for each loop trace. An example is given in Fig. 3.3.

There are many inherent errors in tracing observed post-flare loops by eye. The loops are rarely isolated. The many loops interact and appear to split, converge, and twist. It is possible that some traces started on one loop and ended on another. Thus, we traced a large sample of post-flare loops to limit this error. Another difficulty arose when determining the positions of the footpoints. As plasma interacts with material at the solar surface, its glow brightens and saturates the exposures. Especially where many loops converge, the exact footpoint locations cannot be identified. However, exact locations are not required to identify loop shape.
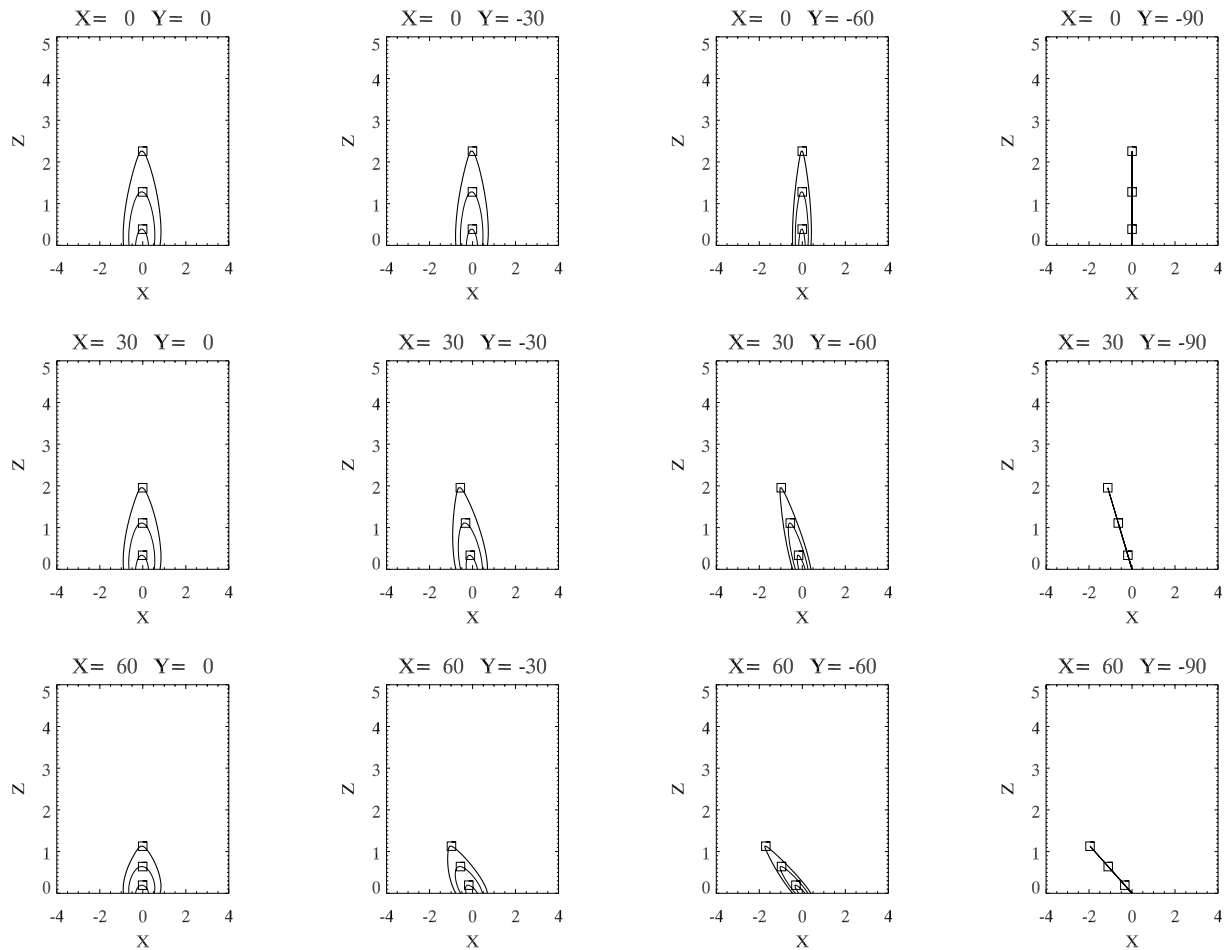
Figure 3.1 Rotations of symmetric post-flare loops about the *X* and *Y* axes. The upper left plot shows no rotation. The three rows, from top to bottom, show rotations about the *X* axis of 0°, 30°, and 60°. The four columns, from left to right, show rotations about the *Y* axis of 0°, −30°, −60°, and −90°. The squares indicate the loop peak (maximum *Z* position of loop). The coordinate positions are dimensionless.
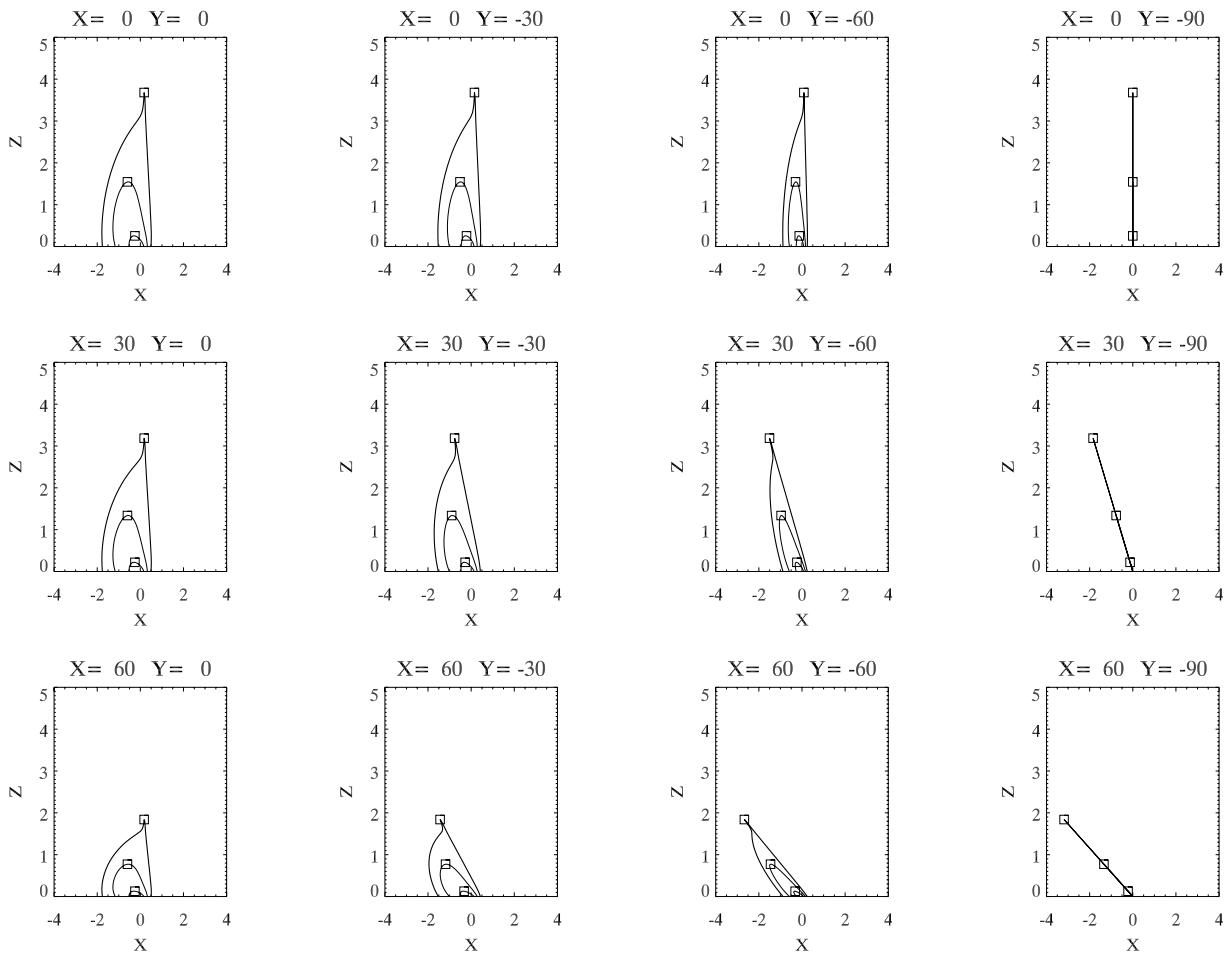
Figure 3.2 Rotations of asymmetric post-flare loops about the *X* and *Y* axes. The upper left plot shows no rotation. The three rows, from top to bottom, show rotations about the *X* axis of 0°, 30°, and 60°. The four columns, from left to right, show rotations about the *Y* axis of 0°, −30°, −60°, and −90°. The squares indicate the loop peak (maximum *Z* position of loop). The coordinate positions are dimensionless.
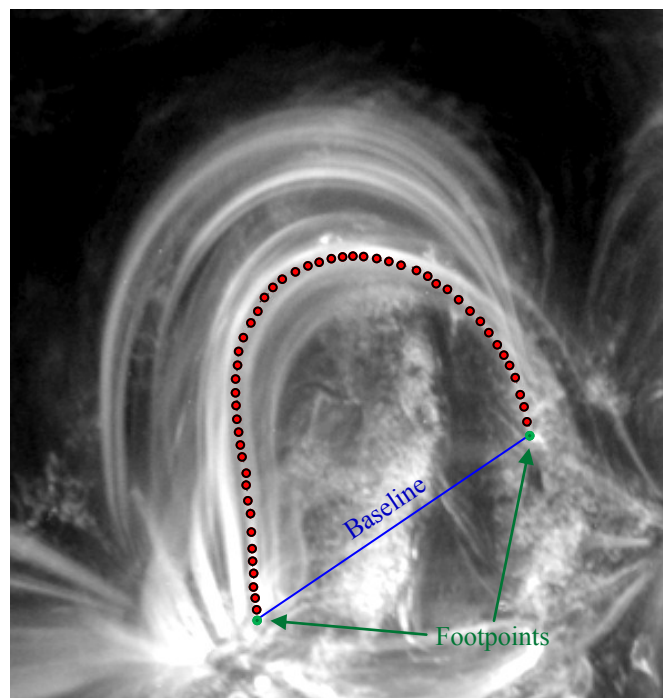
Figure 3.3 An example of tracing a post-flare loop. Each circle represents a single clicked position. The two green circles are the locations of the footpoints where the magnetic field is tied to the photosphere. The line connecting the footpoints is called the baseline.

3.3   Fitting the Simulations to the Observations

We wrote IDL routines that automatically superimpose the simulations onto the observations and determines the goodness of the fit. Since we assumed that the magnetic fields are line-tied, we could match the footpoints from the simulations with the observed footpoints. By measuring the angle and length of the baselines (the line connecting the two footpoints of a loop), the routines calculated the scaling factor and the rotation about the z axis necessary to align the footpoints. This left three free parameters to find the best fit: magnetic field asymmetry, rotation angle about the baseline, and loop height. Loop height is important because taller loops are closer to the x-line and are more distorted.

We used a chi-square algorithm to rank fits. For each point on a simulated loop, it would find the closest point on the traced observed loop. It then summed up the squared distances and divided by the number of points in each loop to determine a goodness factor [see Eq. (3.1)]. The smaller the goodness factor, the better the fit:

$$\text{Goodness Factor} = \frac{\sum_i (\vec{r}_i - \vec{r}_{close})^2}{N_{sim}N_{obs}}. \tag{3.1}$$

Symmetrical simulated loops provide a falsifiable test that the observational loops are asymmetric. Figs. 3.4 & 3.5 show the result of superimposing the symmetrical and asymmetrical simulated loops with the smallest goodness factor onto the traced observed loop of the 2011 eruption event. We did this for 12 traced loops from the 2010 event and 7 loops from the 2011 event. The number of loops each asymmetry fit best is given in Table 3.1. Under no circumstances did a symmetric loop fit better than an asymmetric loop.

3.4   Using STEREO to Constrain Results

To further constrain the free parameters, we rotated the simulated loops onto the plane of STEREO. This did not work perfectly even though we accounted for the rotation angles of the spacecraft, their
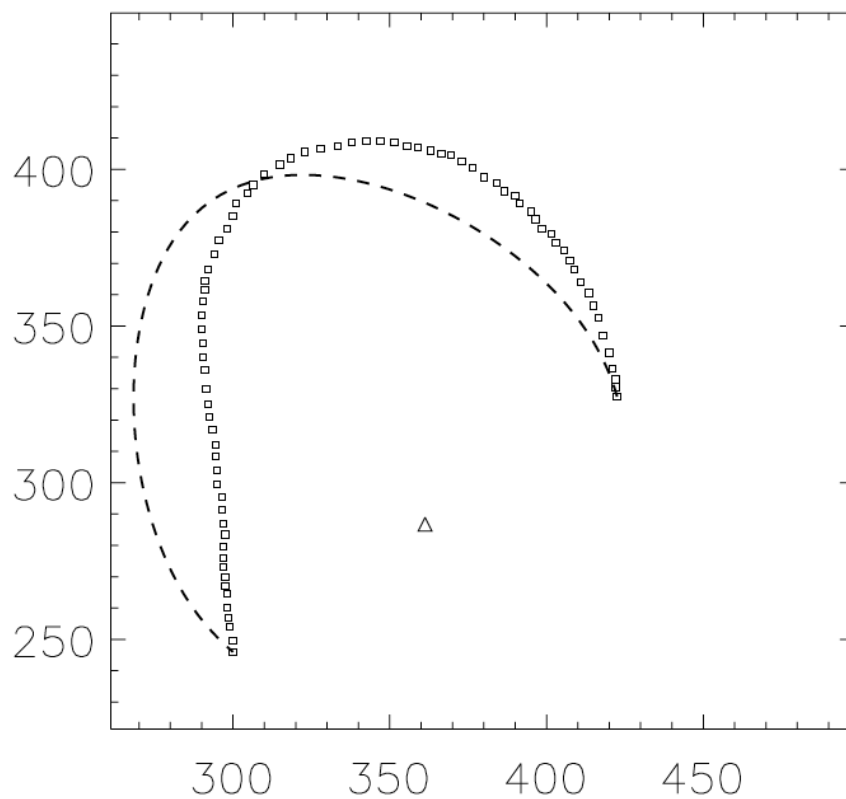
Figure 3.4 Superposition of best symmetric simulated loop onto the 2011 traced observed loop. The axes are pixel positions. The dashed line represents the symmetric simulated loop with the smallest goodness factor. The squares represent the clicked positions tracing a post-flare loop in the 2011 observations. The triangle represents the center of the baseline.
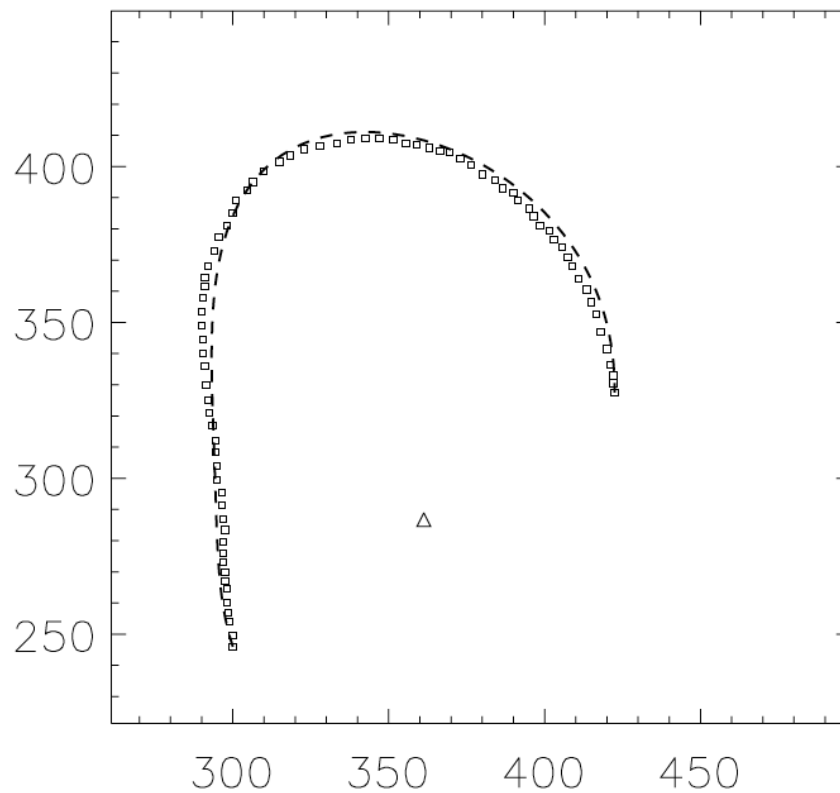
Figure 3.5 Superposition of best asymmetric simulated loop onto the 2011 traced observed loop. The axes are pixel positions. The dashed line represents the asymmetric simulated loop with the smallest goodness factor. The squares represent the clicked positions tracing a post-flare loop in the 2011 observations. The triangle represents the center of the baseline. Note that the loops match well.

Best 2010 Asymmetries	No. of Loops
8:1	5
4:1	2
2:1	1
Best 2011 Asymmetries	No. of Loops
4:1	3
2:1	2
1.5:1	1
1.25:1	1

Table 3.1 The asymmetries that fit observed loops best before loops were rotated into plane of STEREO. For the 2010 event, 12 loops were traced from observed post-flare loops, but only 8 loops were matched by the simulations. For the 2011 event, 7 of 8 simulation loops matched.

distances from the Sun, the radius of the Sun, and the post-flare loops' solar latitude and longitude. After the rotation, we manually adjusted the simulated loops so that the footpoints were aligned with the observed footpoints.

From these rotations, we were able to further constrain the magnetic asymmetries. We noticed that the simulated 8:1 fits for the 6/7 Dec 2010 event did not match the loops in STEREO. However, the 4:1 fits were able to match both the AIA loops as well as the STEREO loops (see Fig. 3.6). Thus, we determined that the magnetic field asymmetry of this event was 4:1, not 8:1. Similarly, the higher asymmetries for the 2011 event did not match the loops in STEREO, which resulted in reducing the magnetic field asymmetry to 1.5:1.
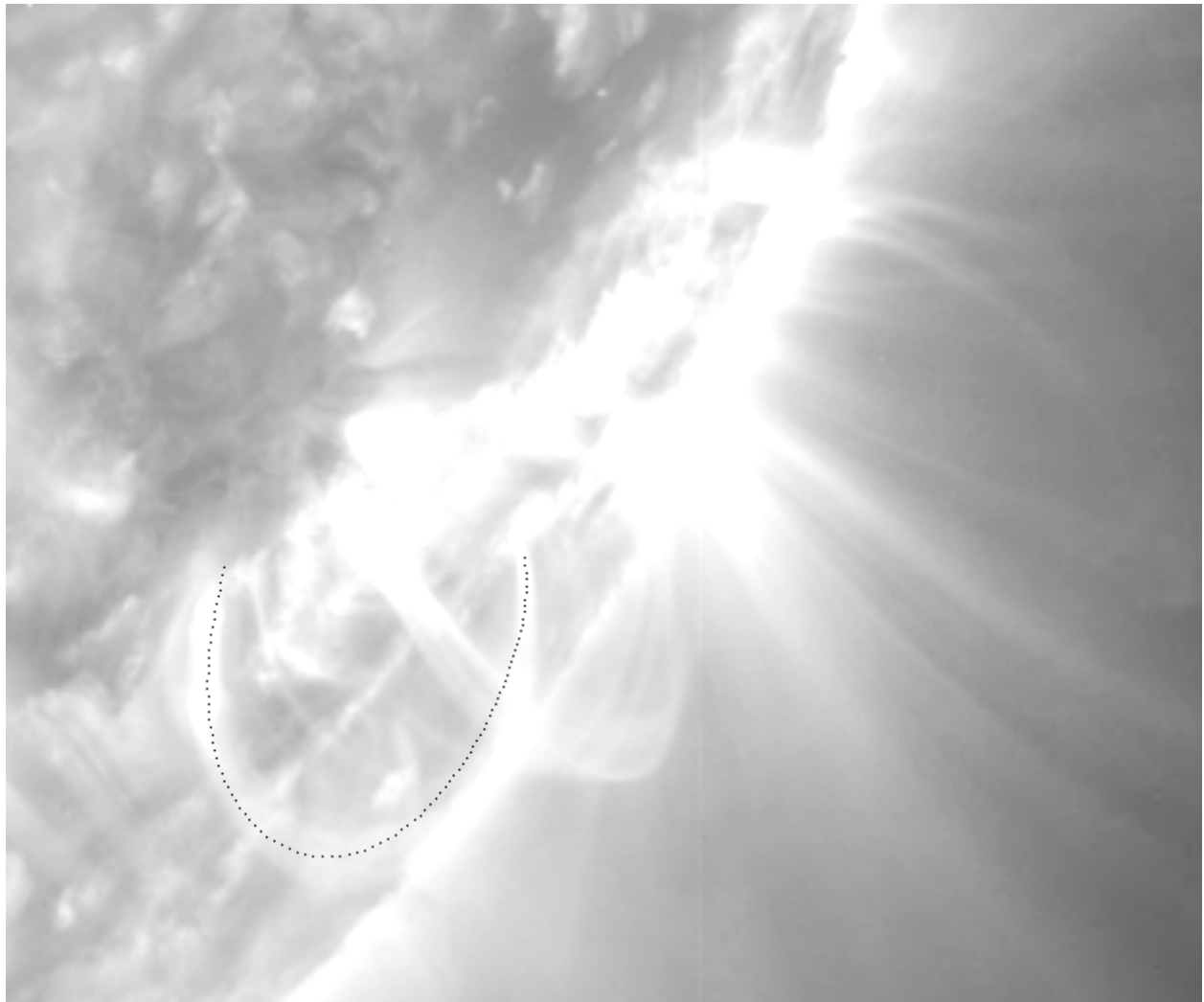
Figure 3.6 Rotation of Simulated Loop onto STEREO for 2010 event. The asymmetry of this loop is 4:1.

Chapter 4

Results and Conclusions

4.1   Results

Of the 19 post-flare loops traced from the observations, 12 were matched by the simulations. The 6/7 Dec 2010 event is consistent with a magnetic field asymmetry of roughly 4:1. The 7 Mar 2011 event is consistent with a weaker magnetic field asymmetry of about 1.5:1.

4.2   Discussion

This project asked three questions enumerated in Section 1.5. The first was can we find evidence of asymmetric magnetic reconnection in solar observations? We answer yes. After we remove projection effects, we find distortion in the post-flare loops. In all cases, the asymmetric loops matched better with observations than symmetric loops.

Second, how well do the simulations agree with observations? About two-thirds of the traced post-flare loops from observations were well fitted by simulated loops. The exceptions exhibited three-dimensional structures and interaction behaviors that the simulations ignore. An example is shown in Fig. 4.1. However, the simulations generally fit isolated loops.
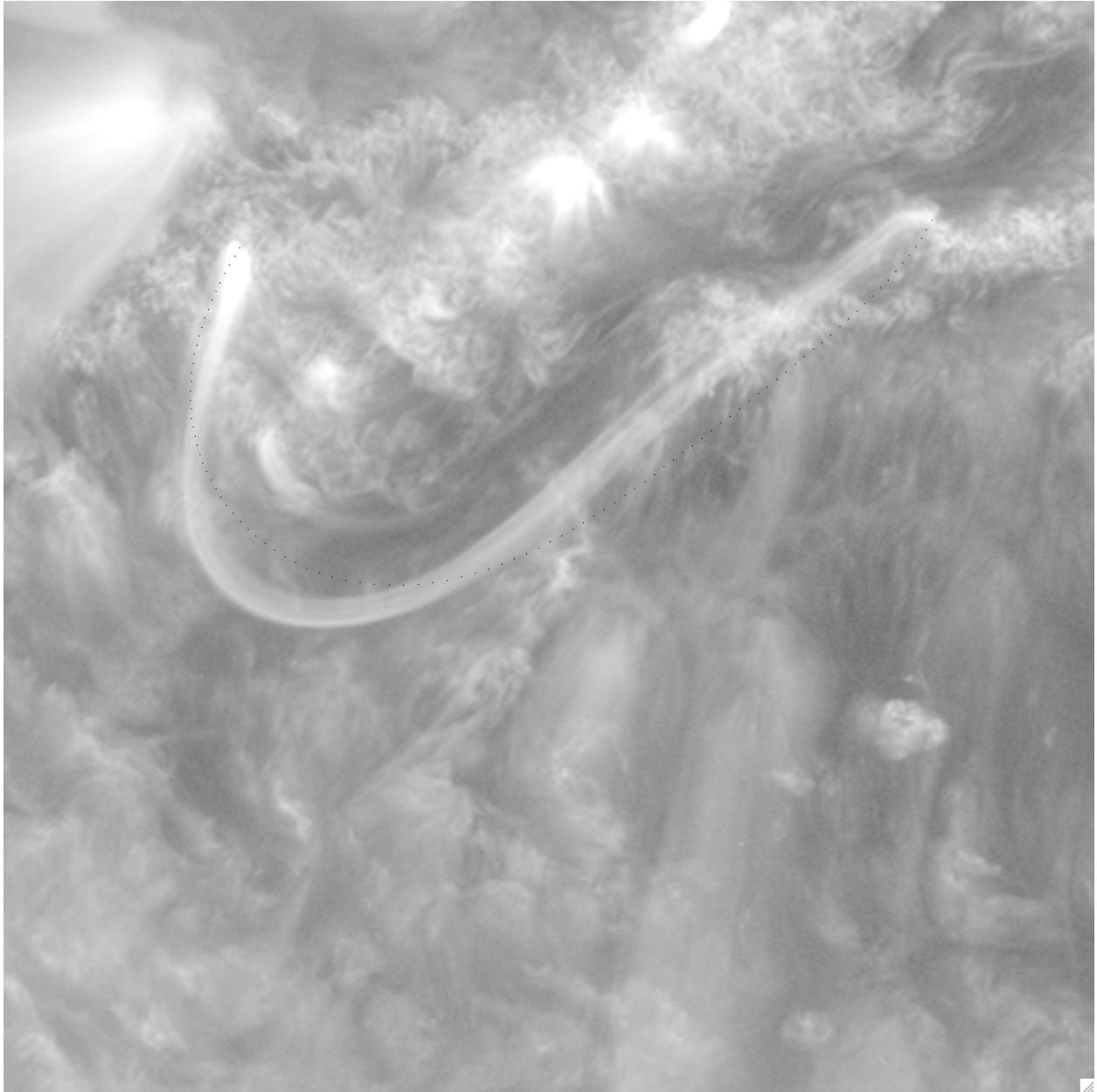
Figure 4.1 No simulated loop could fit this observed post-flare loop. The dotted points show the best fit. The observed loop exhibits a change from positive curvature to negative curvature that could not be reproduced with the NIMROD simulations. This suggests that there is additional magnetic structure that is ignored by the simulations.

Third, can we determine the magnetic field asymmetry during solar eruptions? We can only get a rough estimate. Errors arise from tracing the loops by eye, and free parameters allow multiple simulation asymmetries to fit a single loop. To further constrain the magnetic field asymmetries, we must analyze other signatures of asymmetric magnetic reconnection.

4.3 Directions for Future Work

The method we developed for obtaining magnetic field asymmetries during solar eruption events can be improved. The first step is to update the algorithm that rotates the simulated post-flare loops onto the plane of STEREO. The uncertainties also need to be quantified and reduced. Moving the selected footpoint positions and measuring their effect on the simulated loop fits would quantify the uncertainty inherent to selecting the footpoints by eye. The uncertainties can be further reduced by increasing the number of loops in the study from tens to hundreds.

Distortion in the post-flare loops is only one of the signatures of asymmetric magnetic reconnection (see Section 2.1). Future studies will explore other signatures individually. Combining many of them will further constrain the magnetic field asymmetries and present a story that is more complete.

The magnetic field of the photosphere is measured by HMI magnetograms. Additional work will compare the results of the estimated coronal magnetic field asymmetries with the photospheric ones. These comparisons will provide a better understanding of the magnetic field evolution of solar eruptions.

4.4 Conclusion

We compared simulations of line-tied asymmetric reconnection against observed post-flare loop shapes in order to constrain the magnetic asymmetry during solar eruptions . We found that simu-

lations can match three-quarters of post-flare loop observations. The exceptions showed evidence that the surrounding magnetic field configuration provides additional distortion. By incorporating multiviewpoint observations from SDO and STEREO, we found that the 2010 event is consistent with a magnetic asymmetry of about 4:1 and the 2011 event roughly 1.5:1. This method can be used to estimate the magnetic field asymmetry during solar eruption events. Future work includes combining this method with other signatures of asymmetric reconnection, comparing with photospheric magnetograms from HMI, and investigating a larger sample of events.

By having a method that determines the magnetic field asymmetries during solar eruptions, improved models can be proposed. With better understanding and better models, space weather forecasters may one day be able to predict earthbound solar eruptions.

Bibliography

Ciaravella, A., Raymond, J. C., Li, J., Reiser, P., Gardner, L. D., Ko, Y.-K., & Fineschi, S. 2002, ApJ, 575, 1116

Golub, L., et al. 2007, Sol. Phys., 243, 63

Kaiser, M. L., Kucera, T. A., Davila, J. M., St. Cyr, O. C., Guhathakurta, M., & Christian, E. 2008, Space Sci. Rev., 136, 5

Kosugi, T., Matsuzaki, K., Sakao, T., Shimizu, T., Sone, Y., & Tachikawa, S. 2007, Sol. Phys., 243, 3

Lemen, J. R., et al. 2012, Sol. Phys., 275, 17

McKenzie, D. E. 2011, Phys. Plasmas, 18, 111205

Murphy, N. A., et al. 2012, ApJ, 751, 56

Pesnell, W. G., Thompson, B. J., & Chamberlin, P. C. 2012, Sol. Phys., 275, 3

Phan, T. D., & Paschmann, G. 1996, J. Geophys. Res., 101, 7801

Savage, S. L., McKenzie, D. E., Reeves, K. K., Forbes, T. G., & Longscope, D. W. 2010, ApJ, 722, 329

Sovinec, C. R., et al. 2004, J. Comp. Phys., 195, 355

Su, Y., & van Ballegooijen, A. 2013, ApJ, 764, 91

Warren, H. P., O'Brien, C. M., & Sheeley, Jr., N. R. 2011, ApJ, 742, 92

Yamada, M., et al. 1997, Phys. Plasmas, 4, 1936

Zweibel, E. G., & Yamada, M. 2009, ARA&A, 47, 291

Index